

Article

Integrated Identification of Lithology Using Seismic and Magnetic Anomaly Data for Granite and Gneiss Basement: A Case Study of the LiShui Depression in the East China Sea Basin

Haichao Wu ^{1,2}, Tao Zhang ³, Huafeng Tang ^{1,2,*} , Baoliang Lu ⁴ and Zhe Dong ³¹ College of Earth Sciences, Jilin University, Changchun 130061, China² Key Laboratory of Mineral Resources Evaluation in Northeast Asia, Ministry of Natural Resources, Changchun 130061, China³ Exploration and Development Research Institute, CNOOC Shanghai Branch, Shanghai 200050, China⁴ School of Geological Engineering and Geomatics, Chang'an University, Xi'an 710054, China

* Correspondence: tanghfhc@jlu.edu.cn

Abstract: Granite and gneiss buried hill reservoirs are controlled by their lithology and dark mineral content. Therefore, lithological identification and dark mineral content analysis are important research tools in the early stage of buried hill exploration. In this paper, the relationships between the seismic facies and lithology, magnetic susceptibility, and magnetic anomalies of granite and gneiss are analyzed based on the lithological characteristics of the LiShui depression (LS depression) in the East China Sea Basin (ECSB). The waveform classification method is used to identify granite and gneiss, and the waveform classification results reveal that areas with continuous distribution of a single seismic trace model or two seismic trace models represent good continuity, and can be interpreted as gneiss. Areas with a mixed distribution of multiple seismic trace models represent chaotic and poor continuity, which can be interpreted as granite. The mixed linear zone with multi-seismic trace models is a fault zone, and the rock is cataclasite. In addition, reduction to the pole (RTP) and downward continuation technique for magnetic data processing were used to determine the dark mineral content. Overall, the granite and gneiss can be divided into three types based on magnetic anomaly data: high, moderate, and low magnetic anomaly areas. The areas in which granite with moderate and low magnetic anomalies is distributed are the favorable exploration target areas. The above method provides a technical means of lithological identification in the early stage of buried hill exploration.

Keywords: buried hill; lithology; waveform classification; magnetic anomaly; reservoir



Citation: Wu, H.; Zhang, T.; Tang, H.; Lu, B.; Dong, Z. Integrated Identification of Lithology Using Seismic and Magnetic Anomaly Data for Granite and Gneiss Basement: A Case Study of the LiShui Depression in the East China Sea Basin. *Minerals* **2023**, *13*, 507. <https://doi.org/10.3390/min13040507>

Academic Editor: Paul Alexandre

Received: 13 February 2023

Revised: 17 March 2023

Accepted: 29 March 2023

Published: 1 April 2023



Copyright: © 2023 by the authors. Licensee MDPI, Basel, Switzerland. This article is an open access article distributed under the terms and conditions of the Creative Commons Attribution (CC BY) license (<https://creativecommons.org/licenses/by/4.0/>).

1. Introduction

An important field in oil and gas exploration, granite buried hill reservoirs are widely distributed in basins worldwide [1–7]. In recent years, PL9-1, BZ19-6, YL8-1, and other large oil and gas fields have been discovered in the buried hill areas of offshore basins in China, and thus, granite and metamorphic rock buried hill reservoirs have once again attracted extensive attention [8–11]. The lithologic composition of a buried hill is complex, and this is manifested in two aspects. First, the lithological sequence changes quickly, and many types occur in the transverse and longitudinal directions. Second, the mineral compositions of the rocks are very different [12]. The development of reservoirs is closely related to lithology and mineral composition, and intrusive rocks make better reservoirs than metamorphic rocks [13,14]. Felsic mineral content is positively correlated with porosity, and dark mineral content is negatively correlated with the petrophysical properties of reservoirs [15–18]. This directly affects the formation of fractures and indirectly affects the formation of dissolution pores [19–23]. Therefore, lithological identification and determination of the dark mineral content are of great concern in reservoir evaluation, and comprehensive identification

of geology and logging data, through methods such as conventional logging, image logging [24], the RoqScan real-time wellsite mineral analysis technique [25–27], and mineral component inversion using double indicator curves to identify heavy minerals [28], is carried out during drilling. The lithology of a buried hill can be identified via seismic facies analysis, comprehensive multiple attribute identification, layer velocity analysis [11,29–32], and reconstruction inversion of conventional gamma ray (GR), compensated neutron log (CNL), and density (DEN) logging curves [33,34].

The above research provides a basis for the identification and evaluation of buried hill lithologies. However, in the early stages of exploration, the above methods may not be suitable for lithological identification when few or no wells have been drilled. In this early stage, identification of the lithology and accuracy of the prediction of the dark mineral content are related to the exploration success rate and breakthrough in buried hill exploration. It is necessary to establish a targeted lithological identification method based on 3-D seismic data and magnetic anomaly data that can be used in the early exploration stage. Taking the LiShui depression (LS depression) in the East China Sea Basin (ECSB) as an example (see Figure 1a–c), in this study, the geological and geophysical attributes of the buried hill lithology were analyzed, and geophysical methods of lithological identification suitable for the early exploration of buried hills were investigated, to provide a basis for determining exploration targets and predicting a favorable reservoir distribution area.

Buried hills are topographic highs on basement surfaces in this study. The depth of the boundary between basement and covering formation revealed by the 11 wells in this paper ranges from 1926 to 4099 m. Basement, in this study, is a general term for formations formed before the Cenozoic. The study area was uplifted before the Late Cretaceous and subsided in the Cenozoic, resulting in a lack of formation from the Late Cretaceous to the Cenozoic in the study area. The covering formations of the basement include the Paleocene Yueguifeng, Lingfeng and Mingyuefeng formations, the Eocene Oujiang and Wenzhou Formations, the Miocene Hailong (Longjing) and Yuquan Formations, the Pliocene Santan Formation and the Quaternary Donghai Group from old to young. The Paleocene Yueguifeng Formation is of a lacustrine sequence with thickness of 125–400 m. The Paleocene Lingfeng Formation is of a littoral–neritic sequence with a thickness of 10–480 m, which is mainly composed of primarily gray, dark gray and black mudstones with interbedded thin-layered, light-gray calcareous siltstones, fine sandstones and a few thin-layered calcareous fine sandstones. The Paleocene Mingyuefeng Formation is composed of a regressive sequence with a thickness of 10–750 m, and contains coal beds that were deposited in a delta-plain environment. The lithologic compositions of the formations above the Mingyuefeng formation are mainly mudstone and sandstones [35].

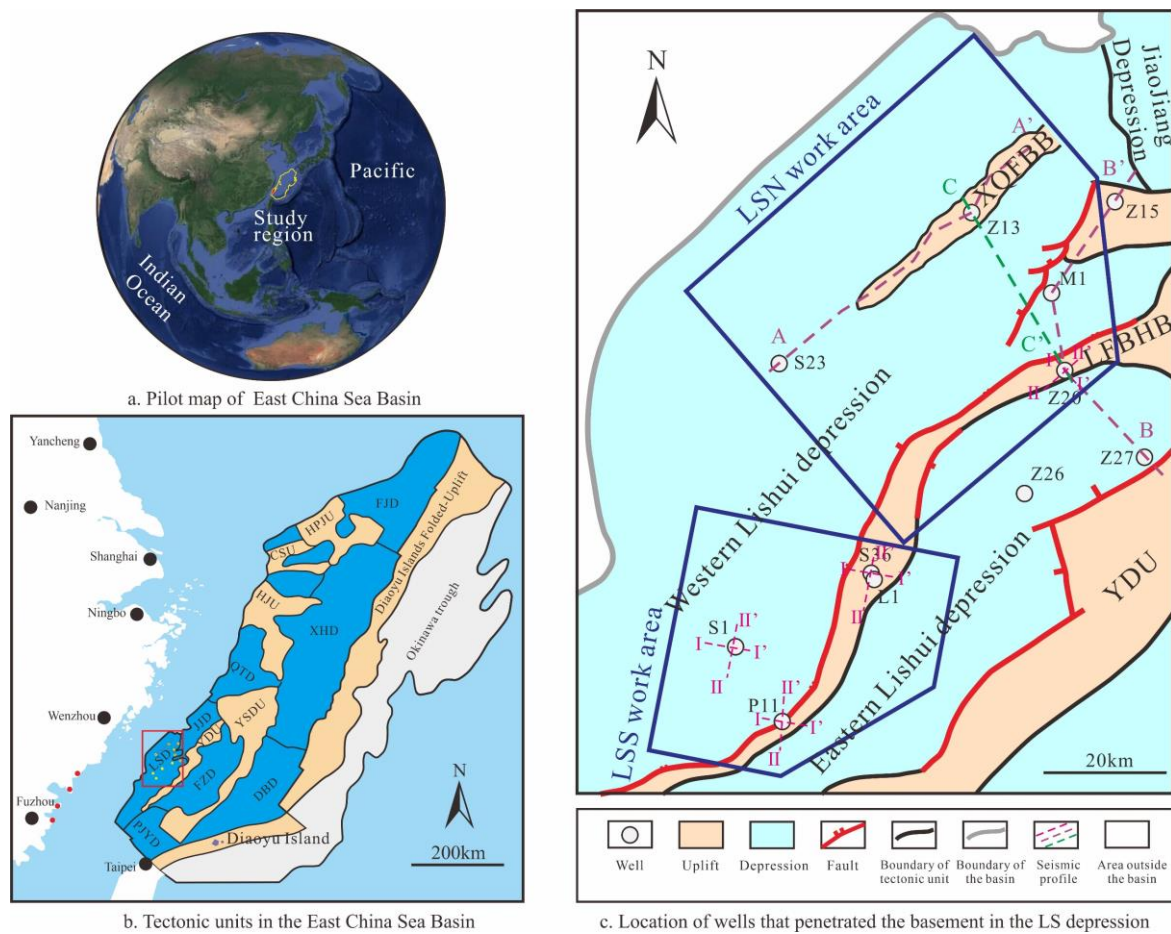


Figure 1. Location of LiShui Depression and wells in study area. Notes: In (a), the yellow line and red zone represent the ECSB and LS depression respectively. In (b), the red rectangle represents the area of (c) in the East China Sea Basin, blue areas represent depressions, beige areas represent uplifts, light blue areas represent areas outside the East China Sea Basin, white areas represent land, red points represent outcrop sampling sites, yellow points represent wells, and colored lines represent seismic profiles. In (c), the blank area in the upper left represents the area outside the basin and the dark blue polygons represent the location of the seismic work area. FJD—FuZhou Depression; HPJU—HuPiJiao Uplift; KSD—KunShan Depression; CSU—ChangShu Uplift; JSBU—JinShanBei Uplift; JSND—JinShanNan Depression; HJU—HaiJiao Uplift, QTD—QianTang Depression; JJD—JiaoJiang Depression; LSD—LiShui Depression; PJYD—PengJiaYu Depression; FZD—FuZhou Depression; YDU—YanDang Uplift; YSDU—YuShanDong Uplift; XHD—XiHu Depression; DBD—DiaoBei Depression. In (c), YDU—YanDang Uplift; XQFBB—XianQiao Fault Block Belt; LFBHB—LingFeng Buried Hill Belt, A–A’ is the location of the seismic profile in Figure 5a, B–B’ is the location of the seismic profile in Figure 5b, C–C’ is the location of the seismic profile in Figure 5c, the I–I’ and II–II’ represent the location of the seismic profiles across wells in Figure 4.

2. Data and Methods

2.1. X-ray Diffraction

A total of 30 samples from the outcrop and drilling cores were tested using X-ray diffraction analysis. X-ray diffraction (XRD) analysis was conducted in the Key Laboratory of Mineral Resources Evaluation in Northeast Asia, Ministry of Natural Resources, Jilin University. According to the sample preparation requirements, 15 g of fresh and clean sample was washed with distilled water, air-dried, finely crushed to 200 mesh using a primary crushing and ball mill, and analyzed after complete mixing. A DX-2007 X-ray diffractometer (Haoyuan Instrument Co., Ltd., Dandong, China) was used to conduct the

analysis, and the peak value of the mineral content intensity was obtained. Mineral content was calculated according to the interpretation process.

2.2. Magnetic Susceptibility

A total of 51 samples from in the outcrop were tested via magnetic susceptibility analysis. An SM-30 portable magnetic susceptibility meter (Orangelamp Geophysical Exploration Co., Ltd, Beijing, China) was used for field measurement of magnetic susceptibility; its maximum measurement sensitivity was 1×10^{-7} SI. During the measurements, a flat and fresh area of rock was selected as often as possible to ensure that the instrument stuck to the rock's surface as much as possible without leaving gaps. Measurement points at different positions were selected according to section length, and each point was measured six to eight times. The data had an error of less than 1% for five replicate measurements, and the geometric average value was taken as the magnetic susceptibility value of the sample.

2.3. Fracture Density

Fracture density, fracture intensity, average fracture spacing, and fracture frequency are all parameters used to assess the degree of fracture development [36]. In this study, we chose fracture density as the parameter to describe the spatial abundance of the fractures. We calculated the fracture density of a total of 30 samples. The statistical method used to determine the fracture density is as follows.

On a field photo of an outcrop containing fractures, a square measuring area was randomly selected to measure the total length of all cracks in the area and the ratio of the total crack length to the area of the measuring area. The equation for calculating the fracture density is

$$F = \frac{\sum Li}{S}$$

where F is fracture density (m/m^2); Li is the length of each fracture in the measuring area (m); and S is the area of the measurement area randomly selected within the region (m^2).

2.4. Seismic Data

A 3D seismic cube of about 4700 km^2 in LiShui Depression was used in the present study. The dominant frequency of the seismic data in the study area was 15 Hz, and its wavelength was 66 ms. The Paradigm was used to process seismic data for the LS work area. Based on its analysis of the seismic facies response characteristics of rocks, the seismic facies analysis method can be used to identify granite and gneiss. Waveform classification is an effective method for seismic facies processing and lithologic facies identification [37,38]. A self-organization neural network approach was used to perform waveform classification and iterative computations to obtain a seismic facies map and predict the lithologic distribution of the basement. The optimal time interval for waveform classification calculations using these data was 33 ms to 132 ms. The time interval selected in this study to perform waveform classification was a time interval that moved down over 120 ms from the top of the basement. According to the model trace computation method for waveform classification based on the Paradigm software manual, we divided the time interval thickness of the layer by six to obtain model traces for the first computation. Fifty percent of the model traces for the first computation were used as model traces for the second computation, and 150% of the model traces for the first computation were used as model traces for the third computation. Through 30 iterations of this computation, 7 and 15 types of model traces were tested. Compared with lithology revealed via borehole cores, it is more reasonable to use the results of the seven types of model traces for lithology interpretation. A self-organization neural network approach was used to perform waveform classification and iterative computations to obtain a seismic facies map and predict the lithologic distribution of the basement. In addition, the vertical lithology of the basement was identified based on characteristics of the vertical seismic facies and well log data.

2.5. Magnetic Anomaly Data

Magnetic anomaly data for the LS depression were obtained from the Global Satellite Magnetic Anomaly Database, which contains data for the latest version (2.0) of the Earth magnetic anomaly grid with a 2-arc-minute resolution model (EMAG2, <http://geomag.org/> (accessed on 12 February 2023)) [39], with a grid size of $2' \times 2'$. Using the acquired magnetic anomaly data, we conducted reduction to the pole and used the downward continuation technique to highlight the magnetic anomaly caused by the basement rocks. Based on the relationship between the reduction-to-pole of the magnetic data and the dark mineral content of the basement rocks, dark mineral content can be estimated to analyze the most favorable area for fracture formation.

3. Lithological Characteristics of the LS Depression

3.1. Lithologic Composition of the Basement in the LS Depression

A total of 11 wells drilled in the study area penetrated the intrusive and metamorphic basement of the basin (see Figure 1c), with a thickness of approximately 1400 m. Identification of basement rocks was conducted based on microscopic identification of 219 thin sections and rock observation results from 18 core samples. Lithology was classified according to genesis and mineral factors, including intrusive and metamorphic rocks. The intrusive rocks are dominated by granodiorite and monzogranite, while the metamorphic rocks are dominated by gneiss and cataclastic gneiss (see Figure 2). Among them, the gneiss was formed in the Late Proterozoic, the granodiorite and monzogranite were formed in the Late Jurassic to Early Cretaceous, and the cataclasite was mainly formed in the stage after the basement outcropped at the surface during the Late Cretaceous. According to the thicknesses of the different lithologies, the specific rock composition is as follows: biotite plagioclase gneiss (46%), monzogranite (40%), and small amounts of granodiorite (5%), syenogranite (4%), biotite schist cataclastic gneiss (3%), and cataclastic granite (2%). Based on the lithologies of the number of wells that penetrated into the basement, only three wells penetrated the gneiss, two of which were only a few hundred meters away from each other. The remaining wells penetrated the granite, so granite was determined to be the main lithology in the plane. XRD results show that the monzogranite is composed of quartz (20–50%), alkaline feldspar (35–50%), plagioclase (45–60%), and biotite (2–10%). The biotite gneiss is composed of quartz (15–30%), alkaline feldspar (30–45%), plagioclase (50–65%), and biotite (3–15%). The total dark mineral content of the gneiss was greater than that of the granite.

3.2. Lithological Association Characteristics of the Buried Hill Revealed by Boreholes in the LS Depression

After identifying the lithologic composition of the basement in the study area through 219 thin sections, we combined 161 thin sections from nine wells with their corresponding geophysical logging data to identify the lithologic associations of the buried hill revealed by the boreholes. There were six types of lithological associations. (1) Monzogranite was drilled in wells S23, Z26, Z27, and M1, revealing the lithology of this area of the buried hill. (2) Monzogranite intercalated with granodiorite was drilled in wells P11 and Z13, revealing the lithology of this area of the buried hill. (3) Equal thicknesses of monzogranite and cataclastic granite were observed to be interbedded in well Z15, revealing the lithology of this area of the buried hill. (4) Granodiorite was drilled in well S1, revealing the lithology of this area of the buried hill. (5) Gneiss was drilled in wells L1 and Z20, revealing the lithology of this area of the buried hill. (6) Gneiss intercalated with cataclastic gneiss was drilled in well S36, revealing the lithology of this area of the buried hill (see Table 1).

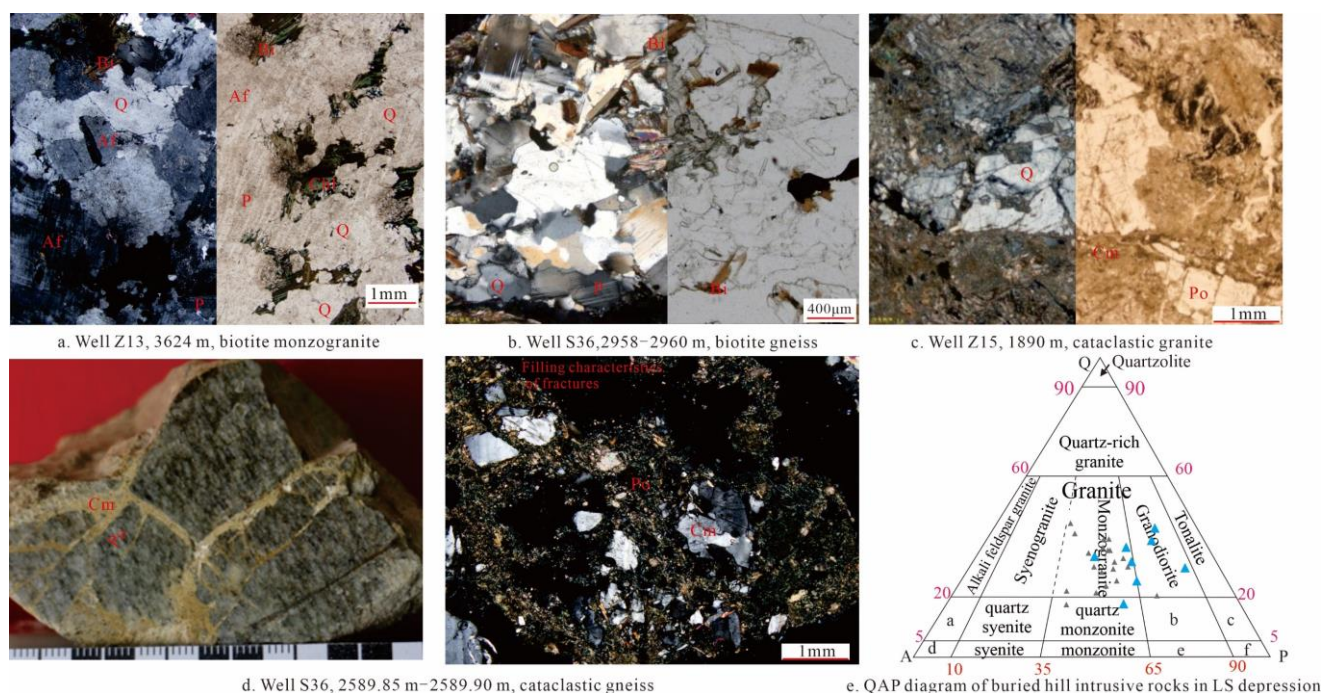


Figure 2. Types of basement rocks in the LS depression in the ECSB. Note: Af—Alkali feldspar, Bi—biotite, Chl—chlorite, P—plagioclase, Q—quartz, Po—porphyroclast, and Cm—cataclastic matrix. Lithology shown in the QAP diagram: a—quartz-alkali feldspar granite; b—quartz monzodiorite, quartz monzonite gabbro; c—tonalite, quartz gabbro, quartz plagioclase; d—alkali feldspar syenite; e—monzodiorite, monzogabbro; and f—diorite, gabbro, plagioclase. In (a–c), the left image is of perpendicular polarized light under a microscope and the right image is of plane polarized light under a microscope. In (d), the left image is a cataclastic gneiss core and the right is a cataclastic gneiss thin section of perpendicular polarized light under a microscope. In (e), the blue triangles denote drilling samples, and the gray triangles denote outcrop samples. Well numbers are abbreviated in this article.

Table 1. Lithologic association of buried hill in the LS depression in the ECSB.

Well	Lithologic Association
S23	Monzogranite
Z26	Monzogranite
Z27	Monzogranite
M1	Monzogranite
P11	Monzogranite intercalated with granodiorite
Z13	Monzogranite intercalated with granodiorite
Z15	Equal thicknesses of monzogranite and cataclastic granite
S1	Granodiorite
L1	Gneiss
Z20	Gneiss
S36	Gneiss intercalated with cataclastic gneiss

Given the limited thickness of the buried hill revealed by the boreholes, the above wells may be incomplete in terms of revealing a single lithology. Because buried hills are characterized by fast changes in lithology in the transverse and vertical directions, it is more reasonable to take complex lithological associations as the main body. Therefore, the types of lithological associations in the study area should be mainly composed of monzogranite interbedded with granodiorite, which are collectively referred to as granite in this paper for convenience; monzogranite and cataclastic granite interbedded with unequal thicknesses; and gneiss interbedded with cataclastic gneiss (see Figure 3).

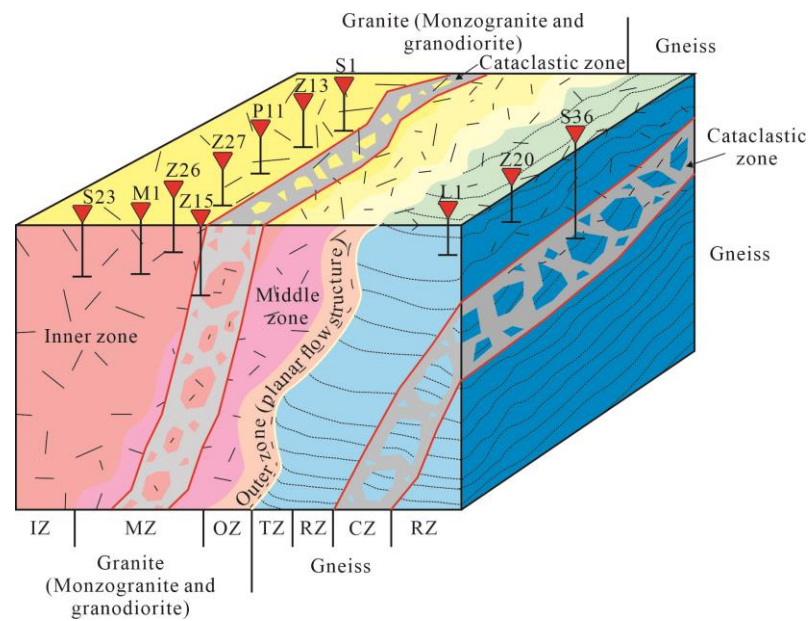


Figure 3. Model of the lithological associations revealed by boreholes in the LS depression, ECSB. Note: IZ, Inner zone; MZ, middle zone; OZ, outer zone; TZ, tilted zone; RZ, regular zone; and CZ, cataclastic zone.

4. Geophysical Response Characteristics of the Lithology

The focus of this study was the relationships between the geological and geophysical properties that can be used to identify lithology via geophysical methods in the early exploration stage, mainly in terms of the seismic facies and magnetic properties.

4.1. Characteristics of Seismic Facies

Seismic facies analysis is often used in lithology and lithofacies identification. The rationality of the lithology or lithofacies interpretation depends on whether the corresponding relationships between the geological attributes and geophysical responses are unique or only apply to a few cases. Seismic facies analysis is usually based on the geometries, seismic reflection configuration, continuity, frequency, and amplitude of seismic reflections [40–42]. Factors that affect the frequency and amplitude include petrologic features, such as the lithology, petrogenetic environment, porosity, and fluid, but may also be caused by seismic imaging. The geometries and seismic reflection configuration are usually determined by the petrologic features and are not easily affected by seismic imaging. Therefore, in lithological identification, it is important to establish the relationship between the lithology and seismic facies identified, using geometry and seismic reflection configuration.

The granite and gneiss buried hill areas have significantly different spatial distributions and seismic reflection configurations. The granite cuts through the host rock; it can form an outer zone with relatively fast condensation and middle and inner zones with slow condensation (see Figure 3). The outer zone is characterized by a planar flow structure and rapid rock density changes, while the middle and inner zones are characterized by a massive structure and small rock density changes. For example, the shape of the GR log curve for well P11 is characterized by a low-amplitude box and micro-teeth, while the density and acoustic log curves are characterized by low-amplitude boxes and are smooth (see Figure 4(A①)). The shape of the GR log curve for well S1 is characterized by a low-amplitude box and micro-teeth, while the density and acoustic log curves are characterized by low-amplitude boxes and micro-teeth. Therefore, the seismic facies in the outer zone of the granite are characterized by a medium amplitude, and those in the inner zone are characterized by a medium-weak amplitude (see Figure 4(A②③, B②③)). This

section is characterized by concentric ring reflections, chaotic or blank internal reflections, and continuous external reflections (see Figure 4(A④,B④)).

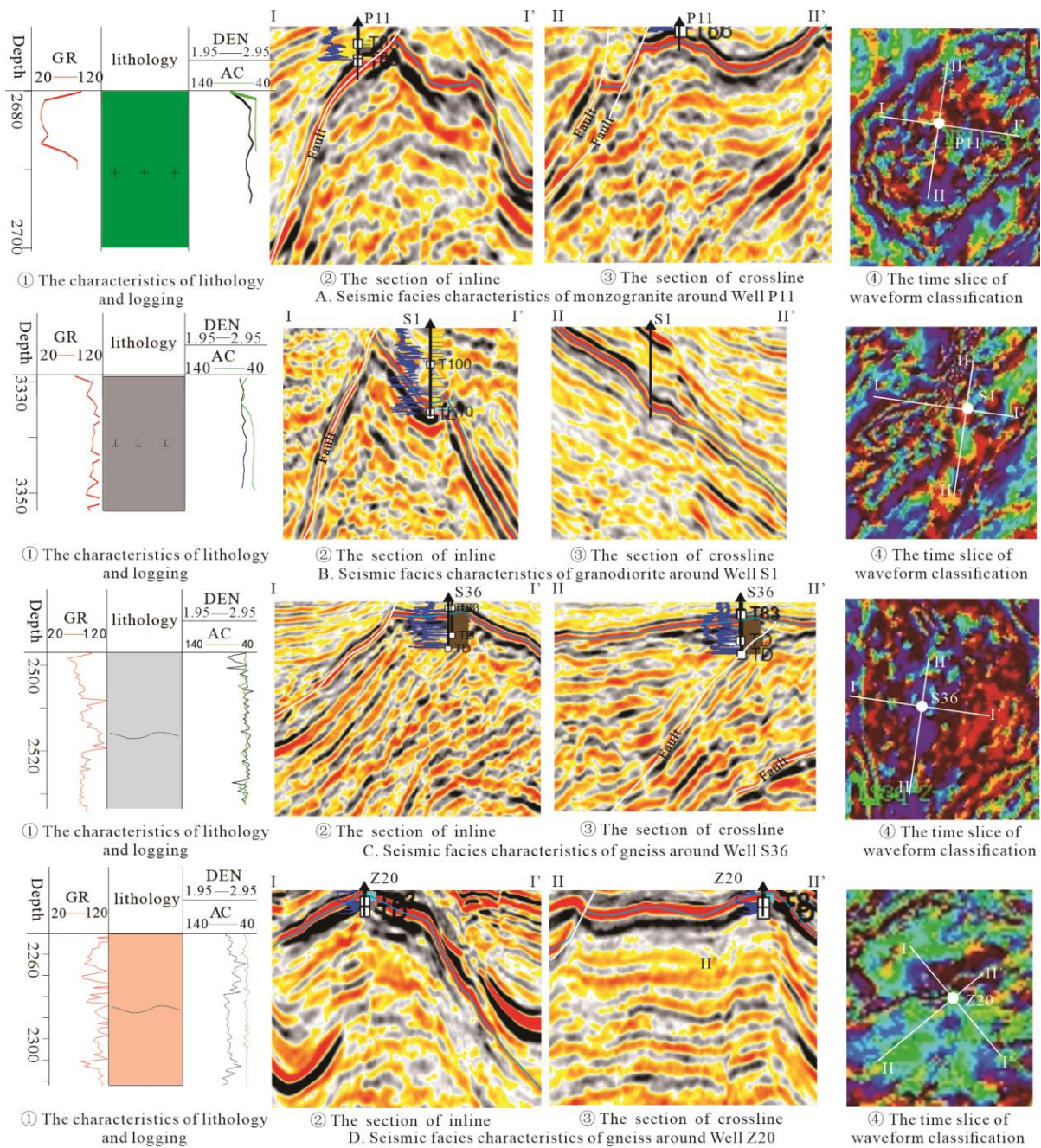


Figure 4. Seismic facies of the basement in typical wells in the LS depression, ECSB. Note: Locations of the wells and seismic profiles are marked in Figure 1c. The arrow in this Figure represents the location of the well. In (A), ① is the logging characteristics and lithology of buried hill of well P11; ② and ③ are the seismic profiles across P11; ④ shows the waveform classification characteristics of well P11 and its surroundings. By analogy, (B) shows the logging characteristics, seismic facies characteristics and waveform classification results of well S1, (C) shows well S36, and (D) shows well Z20.

Due to the density differences among the different minerals, mineral distribution is stratified in the boreholes containing gneiss. For example, the density and acoustic log curves of wells Z20 and S36 are characterized by a low-amplitude box shape and medium-sized teeth (see Figure 4(C①,D①)). Although the gneisses are stratified in the boreholes,

seismic cross sections show that the deformation is strong and the overall structure is pseudo-stratification, so the gneisses have a parallel-subparallel reflection structure (see Figure 4(C②③)). In this area, gneiss is the host rock and is cut through with an uncertain shape. The fault zone has caused fragmentation of the granite and gneiss, and the acoustic and density log curves are characterized by a finger-box shape (see Figure 4(C①)), which causes the geophysical properties of the fracture zone to vary greatly. Therefore, in the inline and crossline, the seismic facies in the section may be relatively continuous in only one direction, while they may be medium continuous-discontinuous in the other direction (see Figure 4(D②③)). The plane section exhibits good continuity (see Figure 4(C④,D④)). The above phenomenon is also obvious in the well tie sections. When a rock mass intrudes, the gneiss in the contact zone is tilted (see Figure 5A,B). In areas where faults are developed, the seismic facies become more chaotic, and their amplitude may become stronger (see Figure 5C).

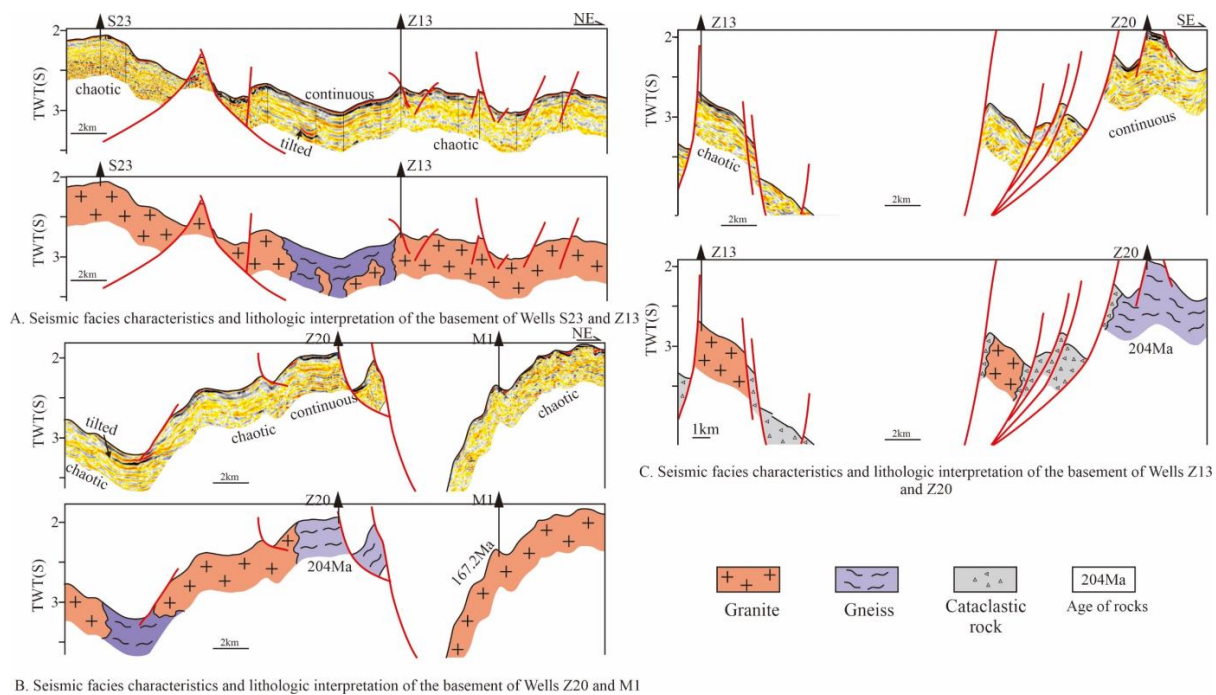


Figure 5. Seismic facies and lithological interpretation of the basement in the LS depression, ECSB. Note: Locations of the three seismic profiles are marked in Figure 1c. In (A), the upper figure is the seismic profile across wells S23 and Z13, while the lower figure is the lithologic interpretation of the seismic profile based on the seismic facies characteristics. By analogy, (B) shows the lithologic interpretation of the seismic profiles of well Z20 and M1, and (C) shows the lithologic interpretation of the seismic profiles of well Z13 and Z20.

4.2. Magnetic Properties of Rocks

Magnetic minerals can be divided into ferromagnetic, strongly paramagnetic, weakly paramagnetic, and diamagnetic minerals. Based on rock-mineral identification and XRD results, the strongly paramagnetic minerals include biotite and hornblende, the weakly magnetic minerals include plagioclase and chlorite, and the diamagnetic minerals mainly include quartz and potassium feldspar. The magnetic field intensity of a rock is mainly affected by the types and contents of magnetic minerals it contains. The magnetic strengths of granite and gneiss are mainly contributed by their strongly paramagnetic minerals.

According to the existing magnetic classification scheme for rocks [43,44], the rocks in the study area can be classified into five types: extremely strongly magnetic, strongly magnetic, medium magnetic, weakly magnetic, and non-magnetic, depending on their magnetic susceptibility values. According to magnetic susceptibility data from core and outcrop samples, core sample test results show that the granite and gneiss exhibit medium

magnetic, weakly magnetic, and non-magnetic characteristics, while outcrop sample test results show that the granite also has strongly magnetic and extremely strongly magnetic characteristics (see Figure 6). By comparing the magnetic susceptibility and dark mineral content, it was found that there is a positive correlation between them (see Figure 7). Considering that the Earth’s magnetic pole has reversed during geologic history, weakly magnetic, medium magnetic, strongly magnetic, and extremely strongly magnetic rocks can produce corresponding negative free-space magnetic anomalies. Therefore, both strongly positive and strongly negative free-space magnetic anomalies correspond to rocks with high dark mineral contents.

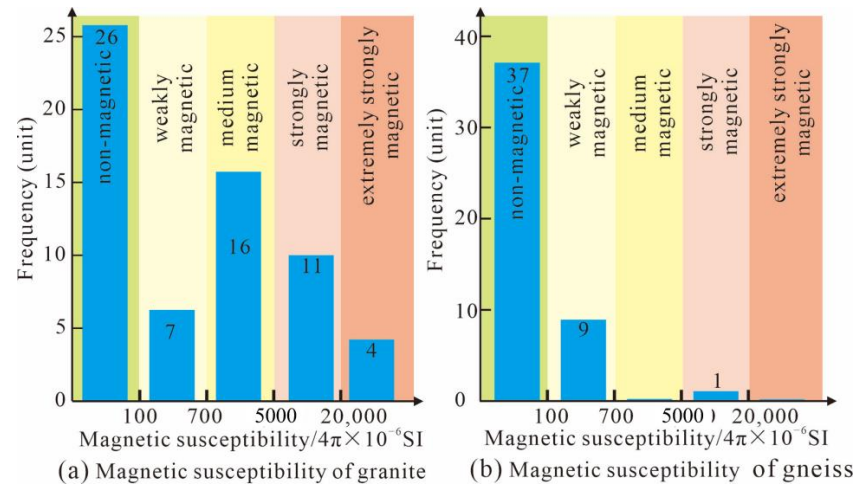


Figure 6. Magnetic susceptibility histograms of granite and gneiss in the ECSB and its adjacent areas. Note: (a,b) show magnetic susceptibility statistics for granite and gneiss samples, respectively.

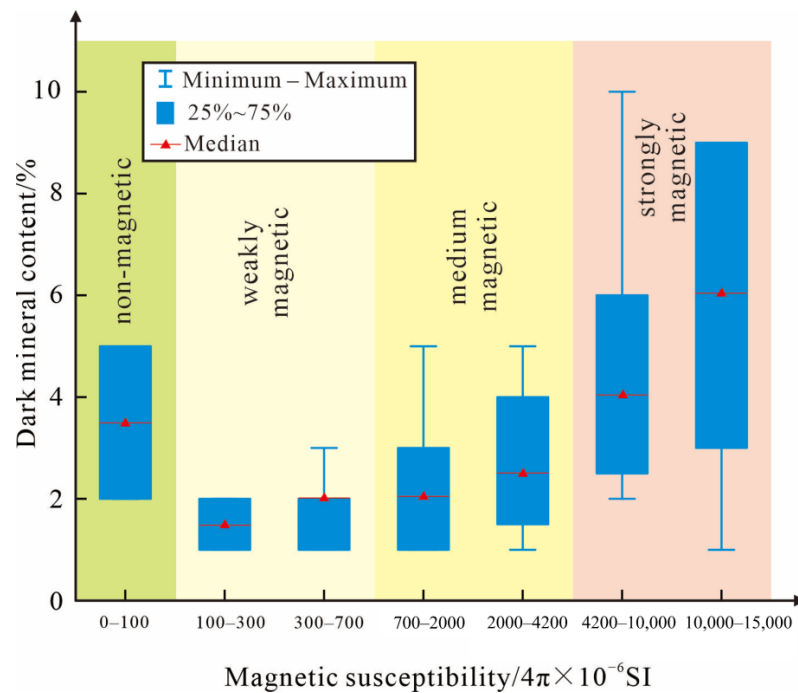


Figure 7. Plot of magnetic susceptibility versus dark mineral content. Note: According to the magnetic susceptibility value, we divided the data into seven ranges and made a boxplot. The median and box data in the figure reflect a positive correlation between dark mineral content and magnetic susceptibility.

5. Lithological Interpretation Based on Geophysical Data

5.1. Lithological Interpretation Based on Seismic Data

The seismic facies can be divided into the following categories based on the waveform classification results. The first is an area with continuously distributed single or two model traces. The second is an area with a mixed distribution of three or four model traces. The third is a strip-like area with a mixture of multiple model traces in the northeast direction. The first model represents features with good continuity that can be interpreted as gneiss. The second model represents disordered, poorly continuous features that can be interpreted as the granite zone (see Figure 8(a-I,b-I)). The third model is a fault zone, where the rock is cataclastic. Attention should be paid to interferences between the third model and the first and second models during interpretation. Through the above methods and calibration of the borehole lithology for lithological interpretation, it was found that granite is the main component of the LSN work area (see Figure 8(a-III)), while gneiss is the main component of the LSS work area (see Figure 8(b-III)).

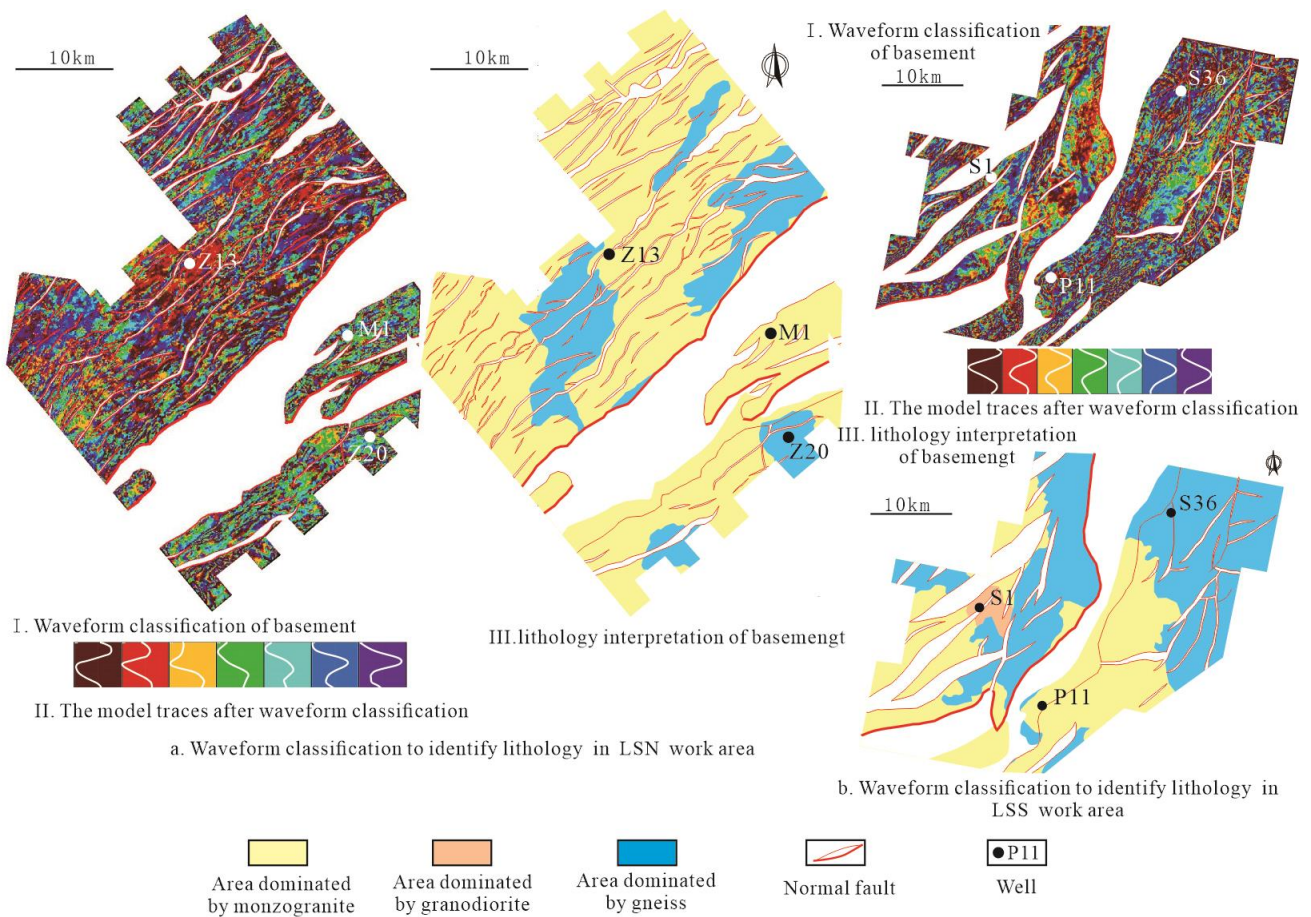


Figure 8. Waveform classification of basement rocks and lithological interpretation in the LS depression. Note: In (a), I is the result of wave classification of basement in the LSN work area, II is the model traces divided by wave classification, and III is the lithology interpretation of basement in the LSN work area based on wave classification. In (b), I, II and III are the same as those in (a), except that the work area is LSS work area.

5.2. Estimation of Dark Mineral Content Based on Magnetic Anomaly Data

Due to limitations on data collection, only satellite data and a small amount of free-space magnetic anomaly data measured by ships were collected in this area, and the free-space magnetic anomaly distribution map was obtained through fusion processing. Based on this, reduction-to-pole was carried out to eliminate the influence of oblique

magnetization. In addition, to highlight magnetic anomalies caused by the basement, reduction-to-pole of the magnetic data was continued downward to 4 km for processing. The absolute value of the magnetic anomaly reaches 750 nT in the LS work area. The maximum absolute value of the magnetic anomaly in the LSN work area is only 150 nT, and the rocks in this area are medium magnetic, weakly magnetic, and non-magnetic rocks (see Figure 9a). The absolute value of the magnetic anomaly in the LSS work area reaches 250 nT, and the rocks in this area range from extremely strongly magnetic to non-magnetic rocks (see Figure 9b). According to the dark mineral contents of the core and outcrop samples, the dark mineral content of the rocks in areas with absolute downward reduction-to-pole magnetic values of 200–250 nT can reach 10–15%, including the monzogranite in well P11 and the granodiorite in well S1. The dark mineral content can reach 5–12% in areas with absolute downward reduction-to-pole magnetic values of 100–150 nT, such as the gneiss in well S36, the gneiss in well Z20, and the monzogranite in well M1. The dark mineral content can reach 5% in areas with absolute downward reduction-to-pole magnetic values of 0–100 nT, such as the monzogranite in well Z13. Comparatively, the low dark mineral content in the LSN work area is conducive to the formation of fractures.

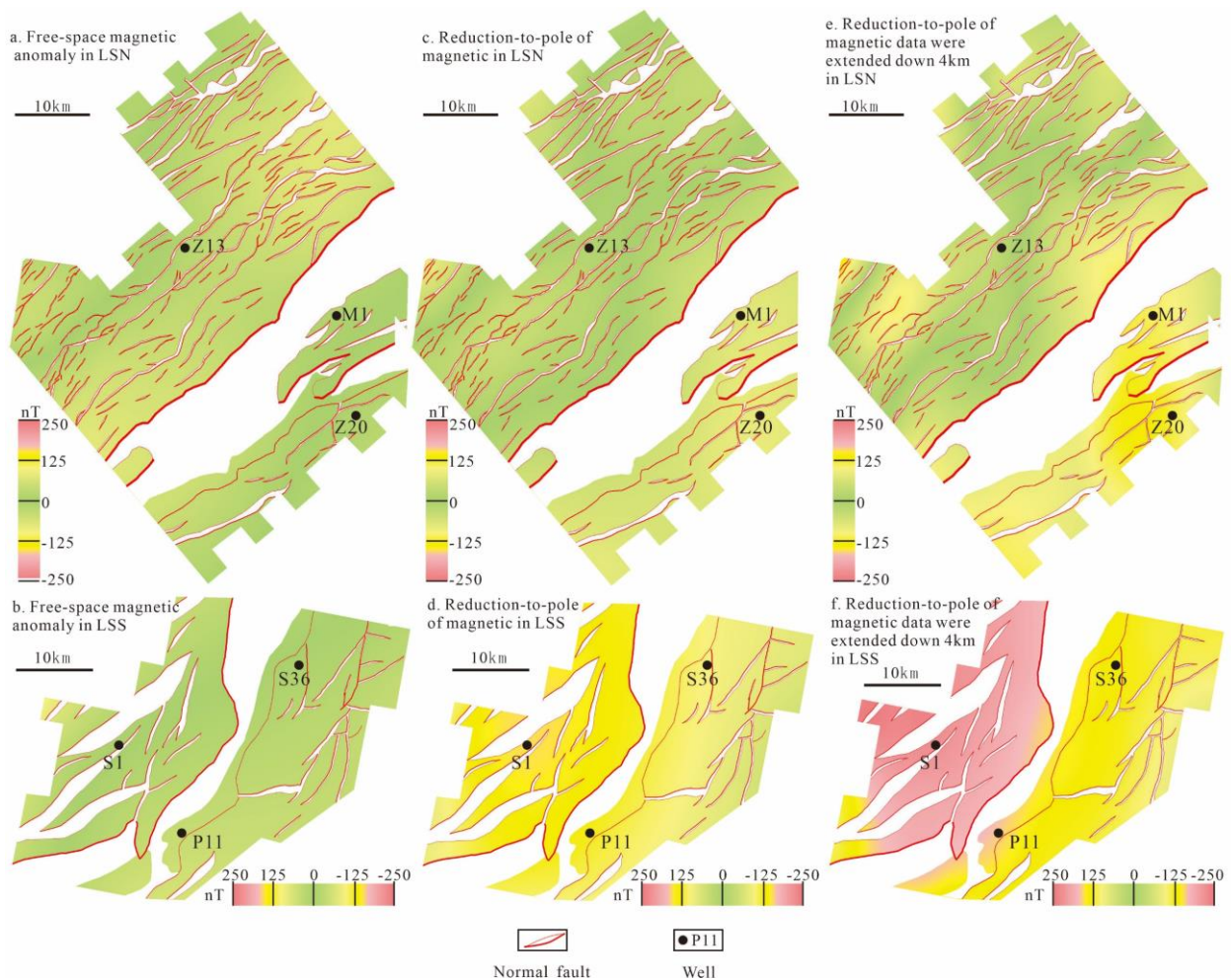


Figure 9. Magnetic anomaly characteristics of basement rocks in the LS depression. Note: (a,b) show the free space magnetic anomaly distribution of the LSN and LSS work areas respectively; (c,d) show the magnetic anomaly distribution of the reduction-to-pole of magnetic in LSN and LSS work areas respectively; (e,f) show the magnetic anomaly distribution of the reduction-to-pole magnetic anomaly data extended down 4 km in LSN and LSS work areas respectively.

5.3. Integrated Interpretation of Pre-Cenozoic Basement Rocks

Based on the waveform classification results and the magnetic identification of the dark mineral content, the basement rock types were divided. The gneiss and granite were divided into three types: those with high (150–200 nT), moderate (100–150 nT), and low (0–100 nT) magnetic anomalies based on the absolute magnetic anomaly values. Absolute magnetic anomaly value is positively correlated with dark mineral content: the higher the absolute value of the magnetic anomaly, the higher the dark mineral content. Overall, the LSN work area is dominated by granite with moderate-low magnetic anomaly intercalated with gneiss with low magnetic anomaly (see Figure 10a). The LSS work area is dominated by granite with moderate-high magnetic anomaly and gneiss with moderate-high magnetic anomaly (see Figure 10b). In conclusion, the distribution of granite and gneiss basement rocks is regional, and the distribution of magnetic anomalies is the same.

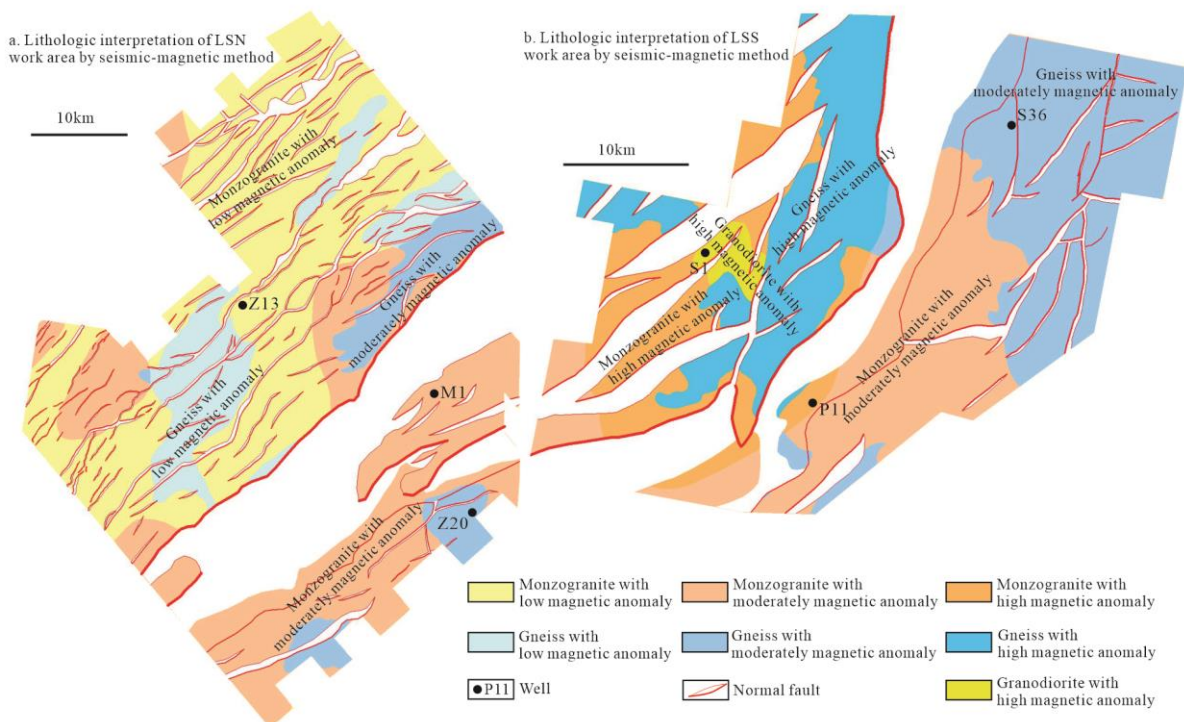


Figure 10. Distribution of basement rocks in the LS depression. Note: (a,b) are lithologic interpretations of basement of LSN and LSS work areas respectively based on the magnetic anomaly distribution magnetic anomaly distribution of the reduction-to-pole magnetic anomaly data extended down 4km and the lithologic interpretation of basement based on waveform classification.

6. Discussion

6.1. Relationship between Lithology and Reservoir

According to the reservoir characteristics revealed by the boreholes, the reservoir space mainly consists of fractures and a few dissolution pores. Tectonic fractures (shear fractures and tensile fractures) and weathering fractures are the main types of fracture. The shear fractures are mainly high-angle and straight fractures, while the tensile structural fractures are jagged and irregular fractures. Both types of fractures were observed in the gneiss section cored in well S36 (see Figure 11a,b). The weathering fractures are mainly network fractures, with variable extension directions, and are often interlaced with major and induced fractures (see Figure 11c). The dissolution pores are mainly intercrystalline micropores produced by chloritization of biotite. Image analysis was conducted to calculate the contributions of fractures and dissolution pores to the reservoir. A total of 53 cast thin sections of gneisses from well S36 were counted, and the results revealed that the fractures contributed 90% to the reservoir, while the dissolution pores contributed only

10% (see Figure 11d). There were fewer granite samples from other wells, and microscopic identification revealed that the gneiss and granite have the same types of reservoir space.

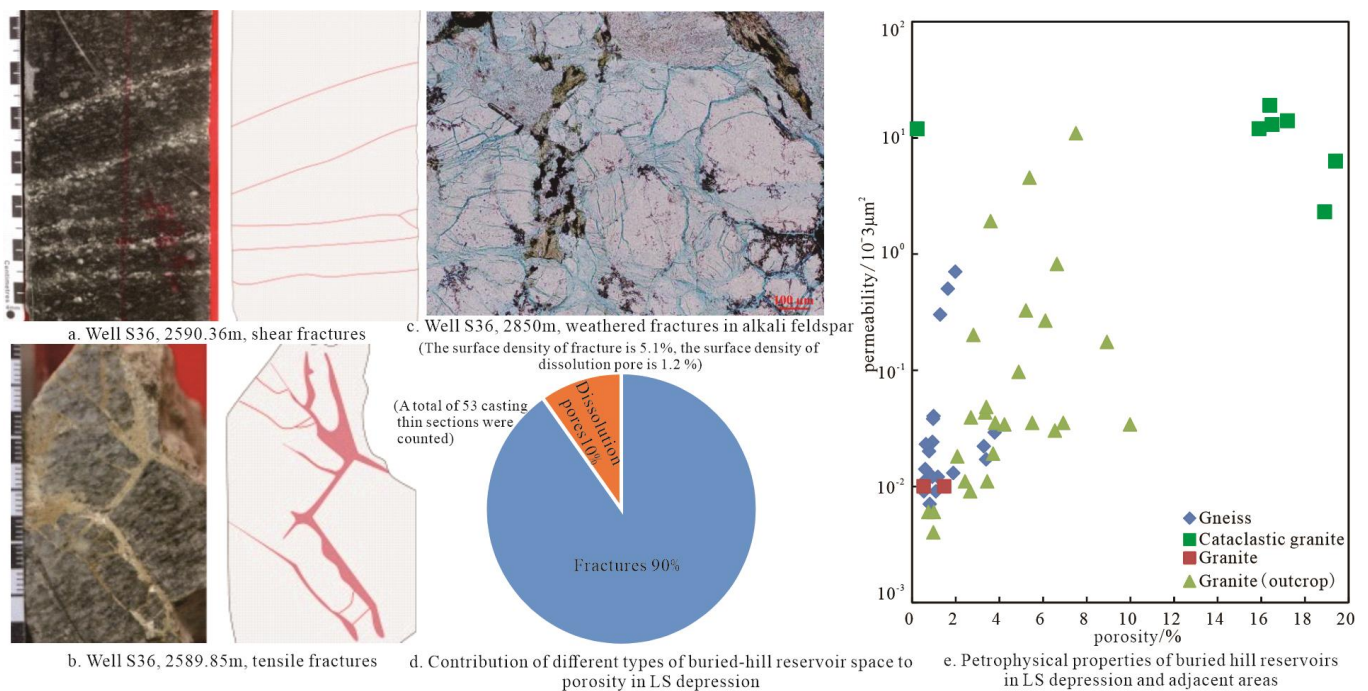


Figure 11. Reservoir characteristics of basement rocks in the LS depression. Note: (a,b) show the fracture characteristics of the core of the buried hill in the well S36, (c) shows the characteristics of the weathered fractures of the core of the buried hill in the well S36, (d) shows the contribution of pores and fractures to the reservoir space of the buried hill, and (e) shows the cross plot of the measured porosity versus permeability of granite and gneiss.

In terms of porosity, the porosity of the granite ranges from 0.2 to 20.8%, with a geometric mean value of 6.2%. Among the granites in the study area, the cataclastic granites have significantly higher porosity. The porosity of the gneiss ranges from 0.55 to 3.8%, with a geometric mean value of 1.2%. Therefore, the porosity of the granite is significantly higher than that of the gneiss. In terms of permeability, the permeability of the granite ranges from 0.01 to 19 mD, with a geometric mean value of 2.5 mD. The permeability of the gneiss ranges from 0.007 to 0.7 mD, with a geometric mean value of 0.03 mD. Therefore, the permeability of the granite is higher than that of the gneiss (see Figure 11e).

In conclusion, the types of reservoir space in the granite and gneiss are similar, but the petrophysical properties of the granite reservoir are better than those of the gneiss reservoir. Therefore, more attention should be paid to the distribution area of granite during exploration.

6.2. Relationship between Rock Magnetism and Fracture

The dark mineral content of the rock can be qualitatively analyzed based on the magnetic anomaly characteristics, and the degree of development of the reservoir can be analyzed according to the reservoir features that are inversely proportional to the dark mineral content. If the relationship between magnetic susceptibility and reservoir development is established, the relationship between magnetic anomaly and reservoir development can be directly established. The development of the granite and gneiss buried hill reservoirs is controlled by fractures, which are beneficial to the development of dissolution and thus affect the development of dissolution pores. The image analysis method was used to analyze the surface density of the fractures. The intersection of the

surface density of the fractures and the magnetic susceptibility revealed that the lower the magnetic susceptibility, the higher the surface density of the fracture, indicating a negative correlation between them. There is a significant difference between granite and gneiss. The surface fracture density of the granite is higher than that of the gneiss (see Figure 12).

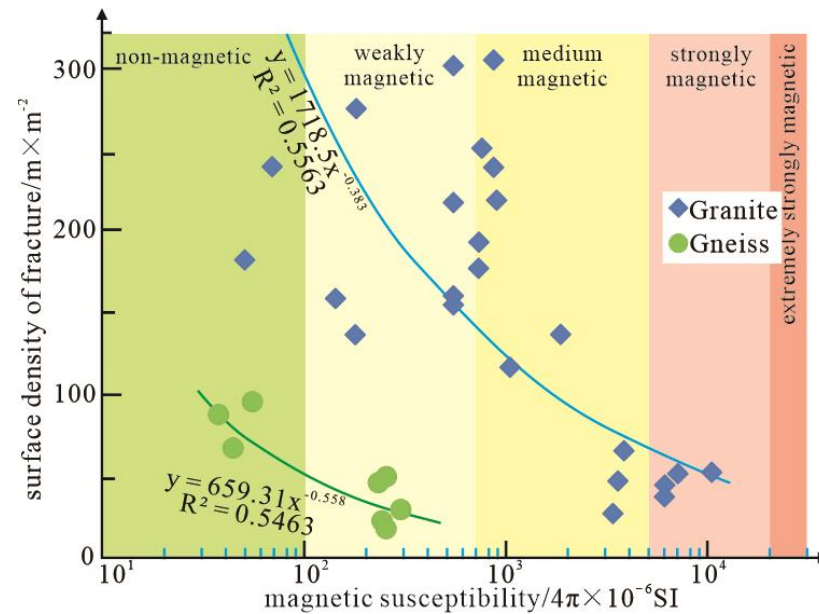


Figure 12. Plot of magnetic susceptibility versus fracture density for basement rocks in the LS depression. Note: Outcrops with measured fracture density were marked with red points in Figure 1b.

According to the above relationships between magnetic anomaly, lithology, and fracture development, fractures are rare in gneiss with a high magnetic anomaly, while a few fractures are developed in gneiss with a low-moderate magnetic anomaly and granite with a high magnetic anomaly. An intermediate number of fractures are developed in granite with a moderate magnetic anomaly, and abundant fractures are developed in granite with a low magnetic anomaly. Therefore, it can be inferred that the fracture development conditions in the LSN work area should be better than those in the LSS work area. It can be seen that gneiss with a high magnetic anomaly is a poor reservoir, gneiss with a low-moderate magnetic anomaly and granite with a high magnetic anomaly are fair reservoirs, granite with a moderate magnetic anomaly is a good reservoir, and granite with a low magnetic anomaly is an excellent reservoir. Therefore, predictions of the distribution of favorable reservoir areas can be made in the LSN and LSS work areas. In the LSN work area, the good and excellent reservoir areas are widely distributed, and the areas of fair and poor reservoirs are similar, accounting for a small proportion. In the LSS work area, the good reservoir areas account for a small proportion and are concentrated in the southern part of the work area. The fair and poor reservoir areas account for a large proportion, and their respective proportions are similar (see Figure 13).

In summary, the most favorable reservoir lithologies of the buried hill in the LS depression are granite with moderate and low magnetic anomalies (i.e., the granites with medium and low dark mineral contents), and more attention should be paid to these two lithologies in exploration.

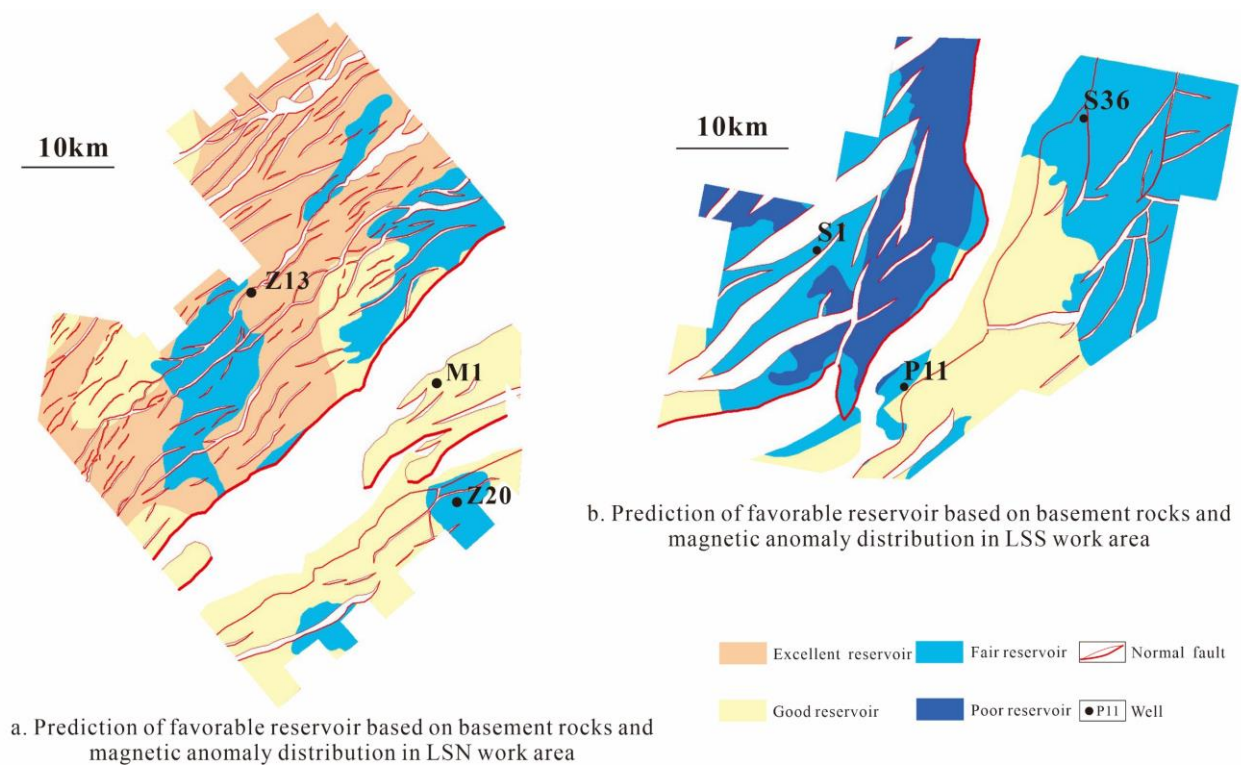


Figure 13. Prediction of favorable reservoir areas based on the basement rocks and magnetic anomaly distribution. Note: Figure 11a,b show the prediction of favorable reservoirs in the LSN and the LSS work areas respectively based on the distribution of magnetic anomalies and basement lithology.

7. Conclusions

1. The basement rocks in the LS depression mainly consist of intrusive and metamorphic rocks. The intrusive rocks are dominated by biotite monzogranite, while the metamorphic rocks are dominated by gneiss and cataclasite. The types of lithological associations in the study area mainly include monzogranite interbedded with granodiorite, interbedded monzogranite and cataclastic granite with unequal thicknesses, and gneiss interbedded with cataclastic gneiss.
2. The seismic facies in the outer zone of the granite are characterized by medium amplitude, and the inner zone is characterized by medium-weak amplitude. The plane section is characterized by concentric ring reflections. The internal reflections are chaotic or blank, and the external reflections are continuous. In the inline and crossline, the seismic facies of gneiss in the section may be relatively continuous in only one direction, while they may be medium continuous-discontinuous in the other direction. In the plane section, it exhibits good continuity. When a rock mass intrudes, the gneiss in the contact zone is tilted. In areas where faults are developed, the seismic facies become more chaotic, and the amplitude may become stronger. Both strongly positive and negative free-space magnetic anomalies correspond to rocks with high dark mineral contents.
3. The waveform classification results indicate that areas with one or two continuously distributed model traces have features with good continuity and can be interpreted as gneiss. Areas with a mixed distribution of three or four model traces have disordered, poorly continuous features and can be interpreted as the granite zone. The strip-like area with a mixture of multiple model traces is a fault zone, and the rock is cataclastic. Using reduction-to-pole and 4 km downward continuation processing of the magnetic data, the magnetic anomaly characteristics of the basement rocks can be determined, and the dark mineral contents of the rocks can be classified accordingly.

4. The types of reservoir space in the granite and gneiss in the study area are similar, but the petrophysical properties of the granite reservoir are better than those of the gneiss reservoir. Magnetic susceptibility is negatively correlated with surface fracture density, and the surface fracture density of the granite is higher than that of the gneiss.

Author Contributions: Conceptualization, H.T.; methodology, B.L.; software, H.W.; validation, T.Z., Z.D. and H.T.; formal analysis, H.T.; investigation, H.W.; resources, H.T.; data curation, T.Z.; writing—original draft preparation, H.W.; writing—review and editing, H.T.; visualization, H.W.; supervision, H.T.; project administration, H.T.; funding acquisition, H.T. All authors have read and agreed to the published version of the manuscript.

Funding: This research was funded by the Key R&D projects in Jilin Province (grant No. 20230203107SF), the National Key R&D Program of China (grant No. 2019YFC0605402) and the National Natural Science Foundation of China (grant No. 41790453).

Data Availability Statement: The data that support the findings of this study are openly available in Geomagnetism at <https://geomag.org/models/emag2.html> (accessed on 12 February 2023), [39].

Acknowledgments: Thanks to the two anonymous reviewers took the time to read this article and put forward their valuable comments.

Conflicts of Interest: The authors declare no conflict of interest.

References

1. Koning, T. Oil and gas production from basement reservoirs: Examples from Indonesia, USA and Venezuela. *Geol. Soc. Lond. Spec. Publ.* **2003**, *214*, 83–92. [CrossRef]
2. Pan, J.; Hao, F.; Zhang, H.-Q.; Wei, P.-S.; Zhang, J.-L. Formation of Granite and Volcanic Rock Reservoirs and Their Accumulation Model. *Nat. Gas Geosci.* **2007**, *18*, 380–385.
3. Cuong, T.X.; Warren, J.K. Bach ho field, a fractured granitic basement reservoir, cuu long basin, offshore se vietnam: A “buried-hill” play. *J. Pet. Geol.* **2009**, *32*, 129–155. [CrossRef]
4. Newton, R.C.; Touret, J.L.R.; Aranovich, L.Y. Fluids and H₂O activity at the onset of granulite facies metamorphism. *Precambrian Res.* **2014**, *253*, 17–25. [CrossRef]
5. Xie, Y.H. Gas resources and accumulation model of BZ19-6 Archean buried-hill large-scale gas reservoir in Bozhong Sag, Bohai Bay Basin. *Pet. Geol. Exp.* **2020**, *42*, 858–866.
6. Zhou, X.H.; Wang, Q.B.; Feng, C.; Ye, T.; Liu, X.J.; Hao, Y.W.; Zhou, L. Formation conditions and geological significance of large Archean buried hill reservoirs in Bohai Sea Earth Science. *Earth Sci. J. China Univ. Geosci.* **2022**, *47*, 1534–1548.
7. Chen, Z.L.; Yin, H.F.; Miao, H.B.; Qiu, Y.C.; Zou, Y. Special bedrock buried hill and the reservoiring process in Qijia-Yitong basin in northeastern China. *Front. Earth Sci.* **2011**, *5*, 191–196. [CrossRef]
8. Xu, S.L.; You, L.; Mao, X.L.; Zhong, J.; Wu, S.J. Reservoir Characteristics and Controlling Factors of Granite Buried Hill in Songnan Low Uplift, Qiongdongnan Basin. *Earth Sci.* **2019**, *44*, 2717–2728.
9. Xue, Y.A.; Wang, Q.; Liu, C.M.; Miao, Q.Y.; Liu, M.X.; Yin, J. Hydrocarbon charging and accumulation of BZ 19—6 gas condensate field in deep buried hills of Bozhong Depression, Bohai Sea. *Oil Gas Geol.* **2020**, *41*, 891–902.
10. Hu, Z.W.; Xu, C.G.; Yang, B.; Huang, Z.; Su, W. Genetic mechanism of the granite buried-hill reservoir of the Penglai 9-1 oilfield in Bohai Sea. *Pet. Res.* **2017**, *2*, 355–365. [CrossRef]
11. Liu, X.J.; Hou, M.C.; Niu, C.M.; Wang, Q.B.; Zhang, X.T.; Ye, T.; Cui, P.Y.; Hao, Y.W. Mesozoic–Cenozoic tectonic controls on the formation of large-scale metamorphic rock buried-hill reservoirs in Bozhong Sag, eastern China. *Geol. J.* **2021**, *56*, 5109–5124. [CrossRef]
12. Zhu, Y.X.; Wang, H.; Shan, J.F.; Yang, C.Y. Reservoir lithology and space characteristics of the Archeozoic basement rock in Ciyutuo buried hill, Liaohe Depression. *Oil Gas Geol.* **2018**, *39*, 1225–1236.
13. Li, J.P.; Zhou, X.H.; Wang, G.Z. Lithologic constitution and its control on reservoir development on Penglai 9-1 buried hill, Bohai Sea Basin. *Earth Sci. J. China Univ. Geosci.* **2014**, *39*, 1521–1530.
14. Xiao, G.J.; Fan, X.Y.; Yu, Z.H.; Yuan, Z.Y.; Destech Publicat, I. In Modeling and Prediction of Fracture-cave Contained in Buried Hill Reservoir, B basin, Central Africa. In Proceedings of the International Conference on Computational and Information Sciences (ICIS), Nanchong, China, 30 May–1 June 2014; pp. 1206–1212.
15. Hao, Q.; Liu, X.; Cha, M.; Li, C.X. Characters and controlling factors on the archean fracture type reservoirs of the Guoyutuo buried hill in the Liao He Basin. *J. Jilin Univ. (Earth Sci. Ed.)* **2006**, *36*, 384–390.
16. Song, B.R.; Hu, Y.J.; Bian, S.Z.; Han, H.D.; Cui, X.D.; Zhang, J. Reservoir characteristics of the crystal basement in the Xinglongtai buried-hill, Liaohe Depression. *Acta Pet. Sin.* **2011**, *32*, 77–82.
17. Wang, D.Y.; Wang, Q.B.; Liu, X.J.; Zhao, M.; Hao, Y.W. Characteristics and developing patterns of gneiss buried hill weathering crust reservoir in the sea area of the Bohai Bay basin. *Acta Petrol. Sin.* **2019**, *35*, 1181–1193.

18. Yu, Z.H.; Du, Y.B.; Xiao, K.Y.; Wang, J.C.; Xiao, G.J.; Zhang, G.L.; Liang, Q.F.; Wang, Y.H. Characteristics and influence factors of basement buried-hill reservoir in Bongor Basin, Chad. *Acta Petrol. Sin.* **2019**, *35*, 1279–1290.
19. Dou, L.R.; Wei, X.D.; Wang, J.C.; Li, J.L.; Wang, R.C.; Zhang, S.H. Characteristics of granitic basement rock buried-hill reservoir in Bongor Basin, Chad. *Acta Pet. Sin.* **2015**, *36*, 897–904.
20. Fan, T.G.; Niu, T.; Fan, H.J.; Hu, G.Y.; Fan, P.J.; Ma, S.F.; Xiao, D.K. Archeozoic buried-hill reservoir of Bozhong 19-6 condensate field: Main controlling factors and development model. *Mar. Geol. Quat. Geol.* **2021**, *41*, 170–178.
21. Hou, M.C.; Cao, H.Y.; Li, H.Y.; Chen, A.Q.; Wei, A.J.; Chen, Y.; Wang, Y.C.; Zhou, X.W.; Ye, T. Characteristics and controlling factors of deep buried-hill reservoirs in the BZ19-6 structural belt, Bohai Sea area. *Nat. Gas Ind.* **2019**, *39*, 33–44. [[CrossRef](#)]
22. Ye, T.; Chen, A.Q.; Niu, C.M.; Wang, Q.B.; Guo, L.L. Characteristics and vertical zonation of large-scale granitic reservoirs, a case study from Penglaioil field in the Bohai Bay Basin, North China. *Geol. J.* **2020**, *55*, 8109–8121. [[CrossRef](#)]
23. You, L.; Xu, S.L.; Mao, X.L.; Zhong, J.; Jiao, Y.Q.; Xiong, X.F. Reservoir Characteristics and Genetic Mechanisms of the Mesozoic Granite Buried Hills in the Deep-water of the Qiongdongnan Basin, Northern South China Sea. *Acta Geol. Sin. Engl. Ed.* **2021**, *95*, 259–267. [[CrossRef](#)]
24. Ye, T.; Niu, C.M.; Wang, Q.B.; Gao, K.S.; Sun, Z.; Chen, A.Q. Identification of metamorphite lithology in paleo buried hill by composition-structure classification: A case study from Archean in Bohai Sea. *Lithol. Reserv.* **2021**, *33*, 156–164.
25. Zhu, J.Y.; Tan, Z.J.; Zhang, G.Q.; Li, D. A comprehensive lithology identification technology for the buried-hill reservoirs with complex lithology in the Bohai Sea. *Oil Drill. Prod. Technol.* **2018**, *40* (Suppl. S1), 62–65.
26. Wang, Y.Z.; Liang, X.; Zhang, J.H.; Chen, Z.H.; Yang, J.J. Depositional controls on mineral assemblage and organic matter accumulation of upper Ordovician–lower Silurian mudstones in northwestern Guizhou area, China. *Int. J. Coal Geol.* **2020**, *231*, 103611. [[CrossRef](#)]
27. Wen, Q.Q.; Yang, X.; Yan, X.L.; Yang, L.S. Evaluation of arsenic mineralogy and geochemistry in gold mine-impacted matrices: Speciation, transformation, and potential associated risks. *J. Environ. Manag.* **2022**, *308*, 114619. [[CrossRef](#)]
28. Zhu, B.Y.; Zhang, C.M.; Zhang, Z.S.; Zhu, L.Q.; Zhou, X.Q. Mineral component inversion of complex lithologic reservoirs in Bozhong 19-6 Archean buried hill. *Lithol. Reserv.* **2020**, *32*, 107–114.
29. Li, J.; Sun, S.L.; Chen, G.P.; Zhang, B.; Hong, L.; He, W.W. Controlling of epimetamorphic rock lithology on basement reservoir and identification of lithological sequence of reservoir in Hailar Basin. *Lithol. Reserv.* **2018**, *30*, 26–36.
30. Zeng, X.P.; Mao, L.; Wang, Y.J.; Yang, J.M. Buried hill lithology identification and reservoir quality forecast in Bonan low uplift. *Spec. Oil Gas Reserv.* **2010**, *17*, 27–30.
31. Deng, Y.H. Formation and characteristics of large-medium buried-hill hydrocarbon reservoirs in Bohai Sea. *Pet. Res.* **2017**, *2*, 97–106. [[CrossRef](#)]
32. Somasundaram, S.; Mund, B.; Soni, R.; Sharda, R. Seismic attribute analysis for fracture detection and porosity prediction: A case study from tight volcanic reservoirs, Barmer Basin, India. *Lead. Edge* **2017**, *36*, 847–960. [[CrossRef](#)]
33. Huang, F.X.; Xia, Z.Y.; Ma, X.L.; Zhao, W.; Gui, Z.X.; Wang, Y. Identification and prediction of metamorphic buried hill lithology based on logging and seismic technology. *Fault-Block Oil Gas Field* **2016**, *23*, 721–725.
34. Wang, S.; Wang, G.W.; Lai, J.; Li, D.; Liu, S.C.; Chen, X.; Yang, K.F.; Song, L.T. Logging identification and evaluation of vertical zonation of buried hill in Cambrian dolomite reservoir: A study of Yingmai-Yaha buried hill structural belt, northern Tarim basin. *J. Pet. Sci. Eng.* **2020**, *195*, 107758. [[CrossRef](#)]
35. Jiang, Z.L.; Li, Y.J.; Du, H.L.; Zhang, Y.F. The Cenozoic structural evolution and its influences on gas accumulation in the Lishui Sag, East China Sea Shelf Basin. *J. Nat. Gas Sci. Eng.* **2015**, *22*, 107–118. [[CrossRef](#)]
36. Ortega, O.J.; Marrett, R.A.; Laubach, S.E. A scale-independent approach to fracture intensity and average spacing measurement. *Aapg Bull.* **2006**, *90*, 193–208. [[CrossRef](#)]
37. Tang, H.F.; Wang, P.J.; Jiang, C.J.; Yu, J.; Liu, W.Z.; Cheng, R.H. Application of waveform classification to identify volcanic facies in Songliao basin. *Oil Geophys. Prospect.* **2007**, *42*, 440–444.
38. Zahraa, A.; Ghosh, D. *Seismic Waveform Classification of Reservoir Properties Using Geological Facies through Neural Network*; Springer: Singapore, 2017; pp. 525–535.
39. Maus, S.; Barckhausen, U.; Berkenbosch, H.; Bournas, N.; Brozena, J.; Childers, V.; Dostaler, F.; Fairhead, J.D.; Finn, C.; von Frese, R.R.B.; et al. EMAG2: A 2-arc min resolution Earth Magnetic Anomaly Grid compiled from satellite, airborne, and marine magnetic measurements. *Geochem. Geophys. Geosystems.* **2009**, *10*. [[CrossRef](#)]
40. Mitchum, R., Jr.; Vail, P. Seismic stratigraphy and global changes of sea level: Part 7. Seismic stratigraphic interpretation procedure: Section 2. Application of seismic reflection configuration to stratigraphic interpretation. *Mem. Am. Assoc. Pet. Geol.* **1977**, *26*, 135–143.
41. Sheriff, R.E. *Seismic Stratigraphy*; Springer Science & Business Media: Berlin/Heidelberg, Germany, 2012.
42. Bischoff, A.; Nicol, A.; Barrier, A.; Wang, H. Paleogeography and volcanic morphology reconstruction of a buried monogenetic volcanic field (part 2). *Bull. Volcanol.* **2019**, *81*, 57. [[CrossRef](#)]

43. Tang, H.F.; Zhao, Z.G.; Tian, Z.W.; Lu, B.L.; Tang, W.; He, K.L.; Zhu, C.X.; Wang, P.J. Characteristics of the Density and Magnetic Susceptibility of Rocks in Northern Borneo and their Constraints on the Lithologic Identification of the Mesozoic Rocks in the Southern South China Sea. *Acta Geol. Sin.-Engl. Ed.* **2021**, *95*, 280–293. [[CrossRef](#)]
44. Saleh, A.; Abdelmoneim, M.; Abdelrady, M.; Al Deep, M. Subsurface structural features of the basement complex and mineralization zone investigation in the Barramiya area, Eastern Desert of Egypt, using magnetic and gravity data analysis. *Arab. J. Geosci.* **2018**, *11*, 676. [[CrossRef](#)]

Disclaimer/Publisher's Note: The statements, opinions and data contained in all publications are solely those of the individual author(s) and contributor(s) and not of MDPI and/or the editor(s). MDPI and/or the editor(s) disclaim responsibility for any injury to people or property resulting from any ideas, methods, instructions or products referred to in the content.